www.springer.com/41230
https://doi.org/10.1007/s41230-025-3113-6
Research & Development
Vol. 22 No. 4 July 2025
CHINA FOUNDRY

Microstructural evolution and comprehensive properties of Mg-8Li-3Al-2Zn alloy during annealing treatment under various cooling rates

Ling Li[1], Wang-yang Xue[2], Zhu-min Li[2], *Tian-yu Liu[3, 4], Rui Zheng[5], and Guo-bing Mao[2]

1. Anhui Engineering Research Center of Vehicle Display Integrated Systems, Anhui Polytechnic University, Wuhu 241000, Anhui, China

2. School of Materials Science and Engineering, Anhui Polytechnic University, Wuhu 241000, Anhui, China

3. Shenyang Research Institute of Foundry Co., Ltd., CAM, Shenyang 110022, China

4. National Key Laboratory of Advanced Casting Technologies, Shenyang 110022, China

5. Shimadzu China Co. Ltd., Shanghai 200233, China

Abstract: Annealing treatment is an effective strategy to enhance the comprehensive properties of Mg-8Li-3Al-2Zn (LAZ832) alloy, where the cooling rate plays a decisive role in tailoring microstructure and performance. This study systematically investigates the effects of cooling rates, controlled via water quenching (WC), air cooling (AC), and furnace cooling (FC), on the phase evolution, mechanical properties, and corrosion resistance of LAZ832. The annealed microstructure consists of α-Mg, β-Li, AlLi, and $MgLi_2Al$ phases, and the volume fraction of Al-Li phases (AlLi and $MgLi_2Al$) increases as the cooling rate decreases. Strengthening mechanisms are dominated by solid solution strengthening, driven by the dissolution of Al and Zn atoms into the matrix, which significantly enhances tensile strength. However, excessive solute content leads to a marked decline in ductility. Scanning probe microscope (SPM) reveals an elevated work function due to the dissolution of Al and Zn atoms into the matrix phase, correlating with improved corrosion resistance. Comprehensive analysis demonstrates that air cooling achieves an optimal balance between tensile strength, ductility, and corrosion resistance, outperforming furnace-cooled samples and offering a pragmatic compromise compared to water-quenched specimens with higher strength but brittle failure. These findings establish a robust framework for designing LAZ832 alloys with tailored microstructures and multi-property optimization, advancing their application in lightweight engineering fields.

Keywords: Mg-Li-Al-Zn alloy; mechanical properties; corrosion resistance; work function; cooling rate

CLC numbers: TG146.22 **Document code:** A **Article ID:** 1672-6421(2025)04-417-10

1 Introduction

Magnesium (Mg) alloys find extensive applications in the industrial field owing to their low density and high specific strength [1-3]. To further pursue reduction of density and enhancement of comprehensive properties, the lighter element, Li, is added into Mg alloys. Magnesium-lithium (Mg-Li) alloys are distinguished as the lightest metallic structural materials, with a density below 1.5 $g \cdot cm^{-3}$ [4, 5]. The introduction of Li reduces the axial ratio (c/a) and leads to the formation of a ductile β-Li phase with a body-centered cubic structure, which substantially enhances the plastic deformation capability. This improvement makes Mg-Li alloys increasingly desirable for applications requiring lightweight and malleable materials [6].

However, the Mg-Li alloy system faces two drawbacks that hinder its broader application. With the increase of Li content, the tensile strength decreases due to the increase of β-Li phase. When the Li content surpasses 10.3wt.%, the tensile strength can fall to approximately 100 MPa, which is notably lower than that of commercially used Mg alloys [7]. Moreover, the already poor corrosion resistance of Mg alloys is further deteriorated with the addition of Li, owing to the highly reactive chemical nature of Li [8, 9].

The multi-componentization design has been proven effective in improving the comprehensive properties

*Tian-yu Liu

Male, Ph. D. His research interests mainly focus on structural modeling of disordered materials, alloy design, and laser additive manufacturing.

E-mail: liutianyusrif@163.com

Received: 2023-09-18; Revised: 2024-02-25; Accepted: 2024-06-02

of the Mg alloys. The addition of Al to the Mg alloy, for example, improves the yield strength and hardening rate during plastic deformation by reducing stacking fault energy and promoting dislocation slipping along the basal plane [5, 10]. The introduction of Zn to the Mg-Li alloy provides a substantial solid solution strengthening effect, enhancing the mechanical stability, ductility, and plasticity of the second phase [11]. Therefore, present research attention is focused on the Mg-Li-Al-Zn alloys. Heat treatment can further enhance the tensile strength of Mg-11Li-3Al alloy to over 400 MPa [12]. Furthermore, the passive film can be formed during the corrosion process due to the dissolution of Al into the matrix phase [13]. In the case of the Mg-8Li-3Al-2Zn-0.5Y alloy, a trade-off between tensile strength and corrosion resistance is achieved, with a maximum tensile strength of 265.7 MPa due to the dissolution of the AlLi phase into the matrix phase [14]. In the Mg-9Li-3Al-1Zn alloy, the synergistic optimization in strength-ductility-corrosion is attained through the introduction of cross-pass friction stir processing [15], facilitated by the unique distribution of the α-Mg/β-Li phases and ultrafine $MgLi_2Al$ precipitates.

The previous studies highlight that the Mg-Li-Al-Zn alloys exhibit a significant improvement in comprehensive properties through multi-componentization design. Nevertheless, it is observed that the Mg-Li-Al-Zn alloys show decreasing plasticity with the increasing content of solutes [16]. Hence, it is necessary to optimize the tensile strength, plasticity, and anti-corrosion properties of Mg-Li-Al alloys.

Generally, the microstructure of a material is influenced by the parameters of heat treatment processes, which can lead to variations in the type, size, and volume fraction of the second phase. These changes subsequently affect the overall properties of the alloys. This study took the Mg-8Li-3Al-2Zn (LAZ832) alloy as the research object. To further explore the effect of cooling rate during annealing treatment on the microstructure and comprehensive properties of LAZ832 alloy, the alloy was subjected to different cooling methods involve water cooling, air cooling, and furnace cooling during annealing treatment. Systematic analyses were conducted on the microstructures, tensile strength, corrosion resistance, and thermal stability induced by different cooling methods. More importantly, the effect of cooling rate on microstructure and comprehensive properties were discussed in detail, unveiling the strengthening mechanism of the alloy. The thermal stability or microstructure homogeneity of the alloy was also assessed using surface potential and work function analysis results. This research provides a theoretical and empirical foundation for refining heat treatment processes and developing high-strength, corrosion-resistant Mg-Li alloys suitable for future commercial and industrial applications.

2 Experimental

2.1 Material preparation

An LAZ832 alloy ingot was prepared by melting pure Mg (99.9%), pure Li (99.9%), pure Al (99.9%), and pure Zn (99.9%) in a vacuum induction furnace under the argon protection. The melt was kept for 7 min at 700 °C before being poured into a steel mold preheated at 200 °C. The resultant as-cast specimens underwent annealing at 350 °C for 270 min within a muffle furnace. Subsequently, different cooling methods, namely, water cooling (WC), air cooling (AC), and furnace cooling (FC) were applied, respectively. The corresponding samples are specifically designated as WC-LAZ832, AC-LAZ832, and FC-LAZ832.

2.2 Material characterizations

The microstructure was observed using the X-ray diffraction (XRD, Bruker D8 Forcus, Karlsruhe, Germany; Cu Kα: λ=0.15406 nm, scanning speed: 4°·min^{-1}). Morphology observations of the sample after etching in 4vol.% nital solution were conducted with an optical microscope (Olympus BX51, Kyoto, Japan) and a scanning electron microscope (SEM, JEOL-7900F, Tokyo, Japan). In-situ composition analysis was performed using an energy dispersive spectroscope (EDS, Oxford INCA X-ACT, Oxford, UK). Surface potential (V_{CPD}) was measured utilizing a scanning probe microscope (SPM, SPM-9700HT, Kyoto, Japan). The relationship between the V_{CPD} and work function can be expressed as follows [17]:

$$V_{CPD}=(\Phi_{tip}-\Phi_{sample})/e \quad (1)$$

where Φ_{tip} and Φ_{sample} represent the electron escape work function of the probe point and the sample surface, respectively. The Φ_{tip} is calibrated by applying highly ordered pyrolytic graphite (HOPG) that possesses 4.7 eV of work function [18], and e is an elementary charge, equal to 1.602×10^{-19} C.

Mechanical properties of the alloys were determined by means of a material test system (UTM5504, Shenzhen, China) at a nominal strain rate of 1×10^{-4} s^{-1} at room temperature (RT). Tensile samples with gage dimensions of 4 mm (width) × 1.5 mm (thickness) ×75 mm (length) were initially cut using electron-discharge machining and then polished on both sides with 2000-grit SiC paper before testing.

Corrosion characterizations were performed with an electrochemical workstation (CHI760E, Shanghai, China). The samples, embedded into epoxy resin with an exposed surface area of 10 mm×10 mm, were immersed in a 3.5wt.% sodium chloride (NaCl) solution at 30±1 °C to serve as an electrolyte solution. A standard three-electrode cell was established, with the samples as the working electrode, platinum as the counter electrode, and Ag/AgCl as the reference electrode. Potentiodynamic polarization measurements were obtained following a 1 h open-circuit potential conditioning, where a scan rate of 1 mV·s^{-1} was applied. Current density and corrosion potential values were determined through the fitting of Tafel curves. Hydrogen evolution and weight loss tests were carried out through immersion tests. The alloy specimens with an exposed surface area of 1 cm^2 were immersed in a 3.5wt.% NaCl solution at 25 °C for 10 h and the volume change of released hydrogen gas with time was recorded. The corrosion morphology was observed and measured using an optical microscope (VHX-5000, Keyence, USA) with a super depth of field.

3 Results

3.1 Microstructural evolution of the annealed LAZ832 alloy under different cooling methods

Figure 1 illustrates the XRD patterns of the LAZ832 alloy subjected to different cooling methods. It is evident that α-Mg+β-Li dual phase structure exists in the as-cast alloy, and the intensity of diffraction peaks of the β-Li phase is stronger than that of the α-Mg phase. Additionally, there are some second phases $MgLi_2Al$ and AlLi, exist in the as-cast alloy. As can be seen in the XRD pattern of WC-LAZ832 alloy, the AlLi phase and $MgLi_2Al$ phase exhibit weaker diffraction peaks comparing to the as-cast alloy, indicating that the precipitates can be dissolved at high temperatures, which aligns with the previous study findings [14]. In the XRD patterns of AC-LAZ832 alloy and FC-LAZ832 alloy, the intensity of diffraction peaks of the AlLi phase and $MgLi_2Al$ phase is stronger than that in the WC-LAZ832 alloy, attributed to the re-precipitation of the two phases with decreasing cooling rate.

The metallurgical structures of the LAZ832 alloy, with and without annealing treatment, are shown in Fig. 2. In the as-cast alloy, it primarily contains α-Mg phase (white regions) and β-Li phase (gray regions), with second phase precipitations mainly distributed in β-Li phase. The α-Mg phase exhibits a predominantly blocky and stripe-like morphology characterized by sharp edges. Following annealing and water cooling, the size of the dispersed α-Mg phase within the LAZ832 alloy decreases, and its edges become more rounded compared to the as-cast condition. This change is due to the rapid cooling rate achieved by water cooling, which limits grain growth. However, when cooling in air or a furnace, the AC-LAZ832 alloy and FC-LAZ832 alloy exhibit coarser grains due to prolonged exposure to high temperatures.

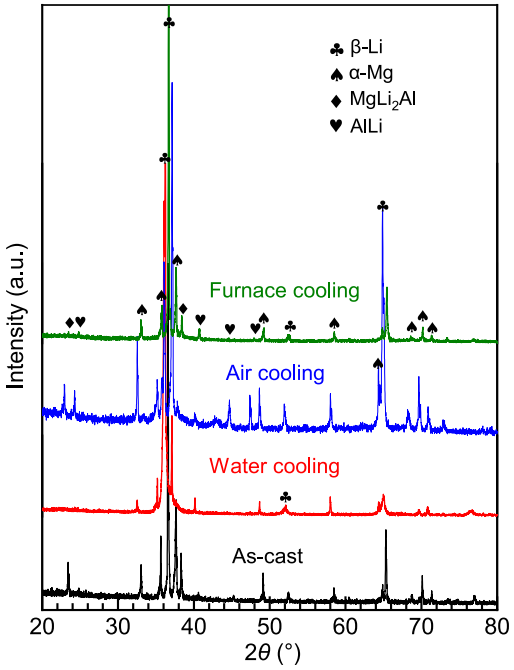

Fig. 1: XRD patterns of LAZ832 alloy under different cooling methods

To provide a clearer view of precipitation distribution, SEM/EDS analysis was performed, as shown in Figs. 3 and 4. These analyses confirmed that the island phases consist of α-Mg, which is consistent with the metallurgical structure of

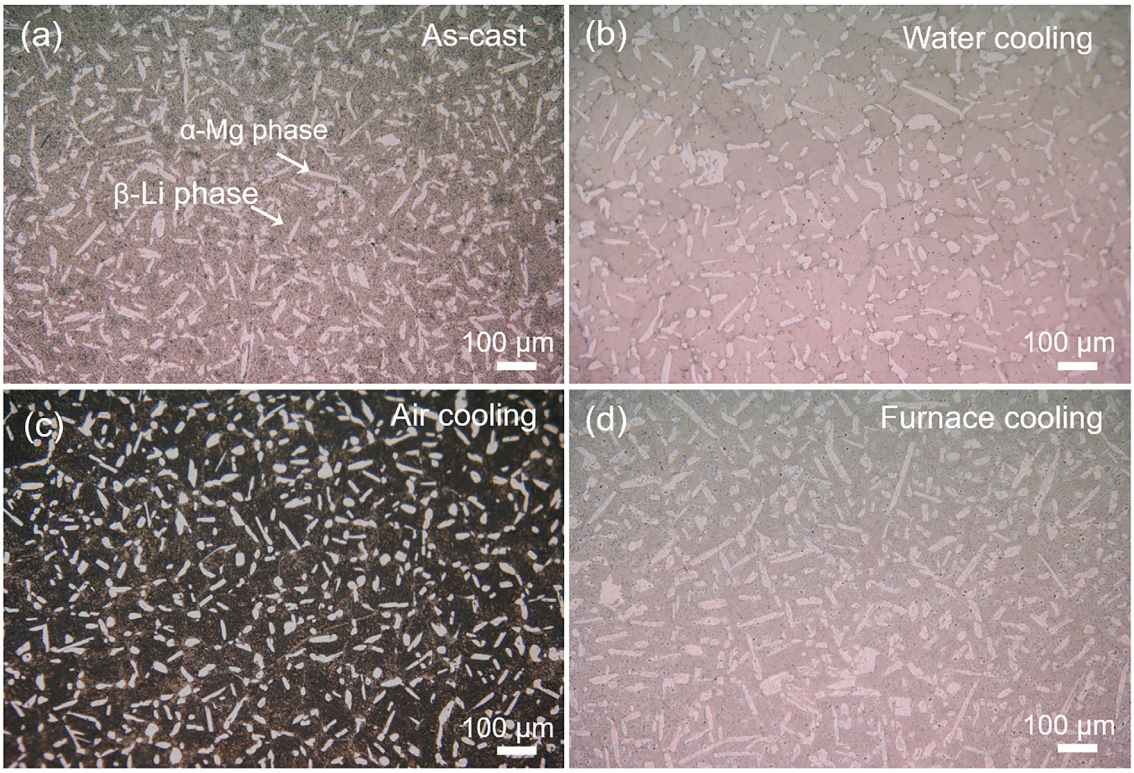

Fig. 2: Metallurgical structures of LAZ832 alloy with and without annealing treatment: (a) as-cast; (b) water cooling; (c) air cooling; (d) furnace cooling

the as-cast alloy, while the matrix is primarily composed of β-Li. Additionally, large-sized particles were noted along the interface between the α-Mg and β-Li phases, with spherical particles present within the β-Li matrix. XRD and EDS analysis confirm both the large-sized irregularly shaped particles and spherical particles can be identified as an AlLi phase with Zn dissolution [Fig. 4(a)]. It is noteworthy that the EDS cannot detect the presence of Li elements because of the

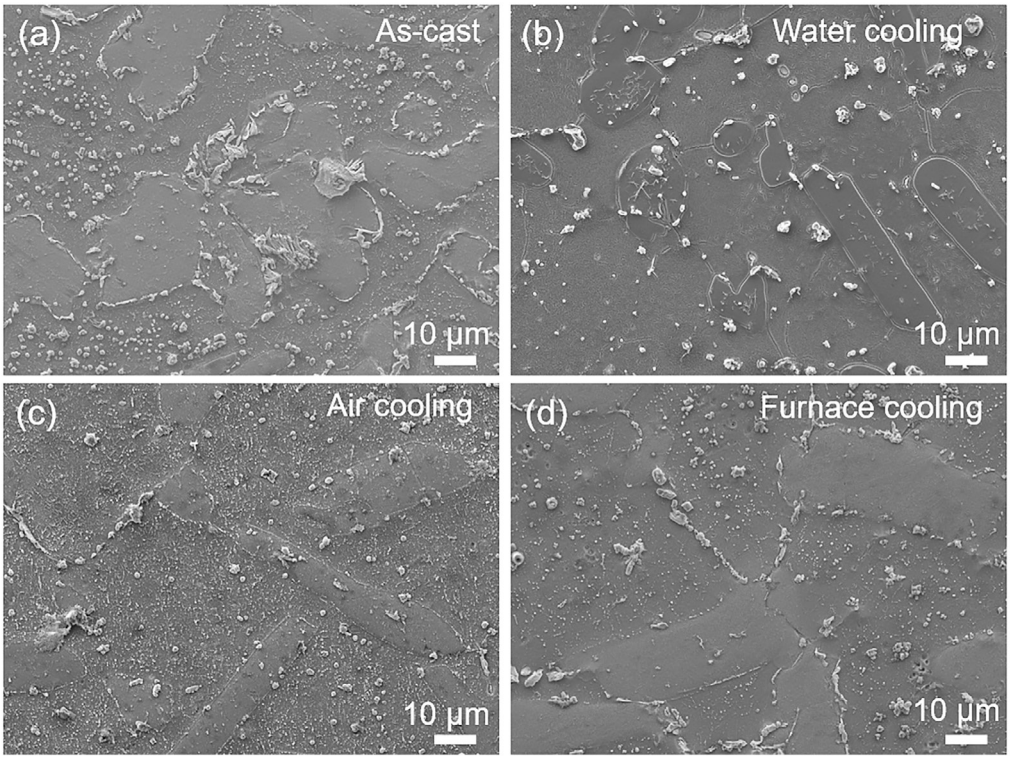

Fig. 3: SEM secondary electron images of LAZ832 alloy with or without annealing treatment: (a) as-cast; (b) water cooling; (c) air cooling; (d) furnace cooling

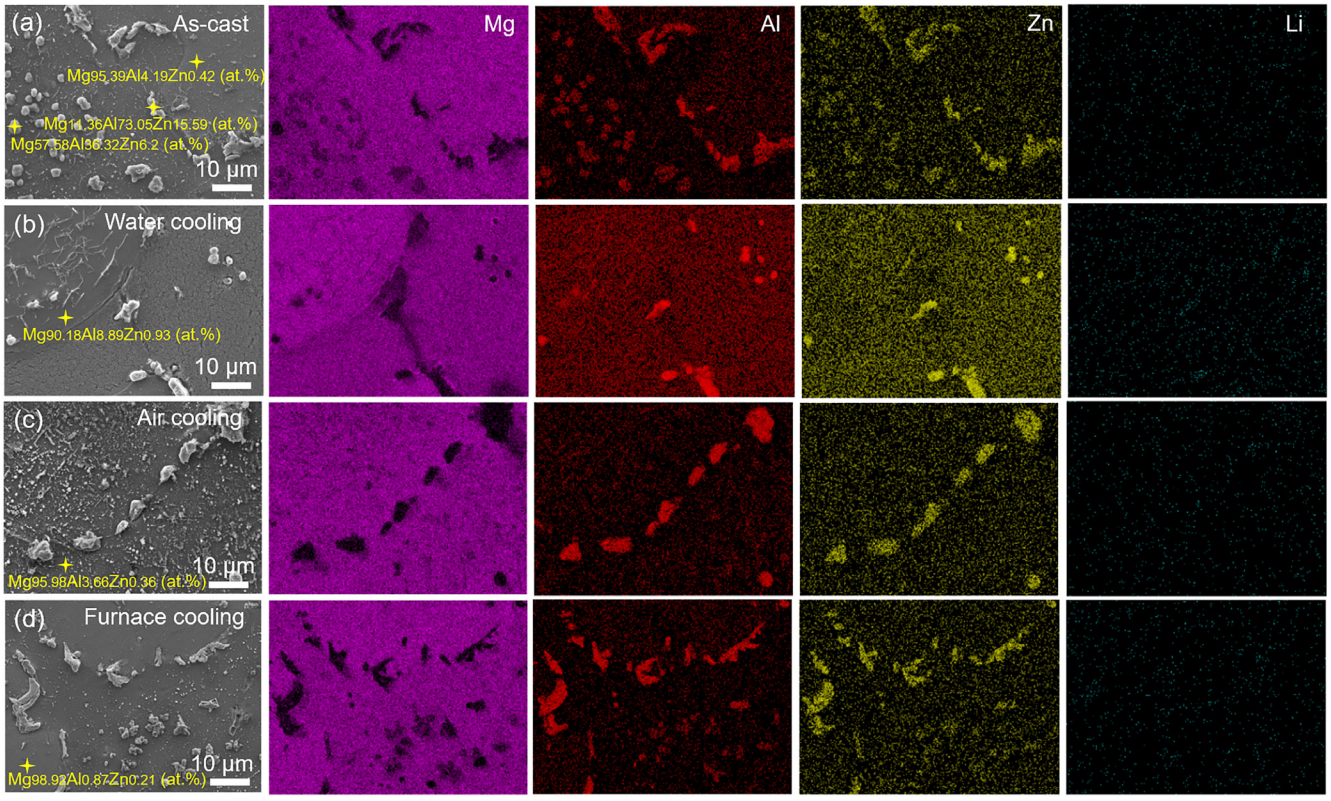

Fig. 4: Point composition analysis and in-situ EDS single element mappings of LAZ832 alloy with and without annealing treatment: (a) as-cast; (b) water cooling; (c) air cooling; (d) furnace cooling

spectrum cutoff for elements with atomic numbers below that of boron. Furthermore, some ultra-fine particles existing in the β-Li or α-Mg are tentatively identified to be $MgLi_2Al$ phases based on the XRD analysis and the related studies [19, 20].

The EDS analysis results of the matrix phase show there is a higher concentration of Al and Zn atoms dissolved in the matrix of WC-LAZ832 alloy. With a decrease in cooling rate, the content of Al and Zn diminishes. This is because Al and Zn atoms have a tendency to cluster rapidly, subsequently forming the $MgLi_2Al$ phase. With a slower cooling process, this phase gradually transforms into the AlLi phase [15, 21]. Therefore, FC-LAZ832 alloy exhibits a higher volume fraction and larger size of the AlLi phase, whereas the values reduce when the alloy is cooled in air. The WC-LAZ832 alloy shows a minimum value in the volume fraction and size of the AlLi phase.

3.2 Mechanical properties and fracture behavior of the annealed Mg-8Li-3Al-2Zn alloy under different cooling methods

Figure 5 depicts the engineering stress-engineering strain curve, ultimate tensile strength (σ_{UTS}), yield strength (σ_{YS}), and elongation (δ) of LAZ832 alloy with or without annealing treatment. In the as-cast alloy, the values of σ_{UTS}, σ_{YS}, and δ are 169 MPa, 145 MPa, and 17%, respectively. However, when cooled in water, the measured values are 280 MPa, 268 MPa, and 4.9%, respectively, with the value of δ being the lowest. In contrast, when cooled in air, the values of σ_{UTS} and σ_{YS} decrease to 202 MPa and 183 MPa, respectively, while the value of δ increases to its peak value of 23.9%. With a decrease in cooling rate, all values of the specimens, σ_{UTS}, σ_{YS}, and δ, reduce to 170 MPa, 158 MPa, and 5.7%, respectively. The variation in mechanical properties is intricately related to the microstructural evolution, such as the variation of solid solution degree, type, shape (including size), and volume fraction of precipitated phases. The details will be presented in the discussion section.

Figure 6 shows the tensile fracture morphology of the Mg-8Li-3Al-2Zn alloy with and without annealing treatment. In the fracture surface of the as-cast alloy, as shown in Fig. 6(a), several small and shallow dimples and some cleavage planes are evident. Each dimple conceals a cracked secondary phase, serving as the nuclei of the crack generation within the matrix [14]. Annealing treatment and subsequent cooling in water transform the fracture mode of the alloy from a ductile fracture to a brittle fracture, and numerous dimples disappear, as shown in Fig. 6(b), aligning with the tensile test results. In comparison, the AC-LAZ832 alloy demonstrates similar fracture characteristics to those of as-cast alloy, yet for the AC-LAZ832 alloy, more dimples are observed and the cleavage planes gradually decrease, as shown in Fig. 6(c), indicating improved elongation. However, with a further decrease in cooling rate, an increased number of cleavage planes and decreased dimples are observed in the FC-LAZ832 alloy, resulting in a lower elongation compared to the as-cast alloy and AC-LAZ832 alloy.

3.3 Corrosion behaviors and corrosion morphology of the annealed LAZ832 alloy at different cooling rates

The polarization curves of as-cast and annealed LAZ832 alloys after immersion for 60 min are presented in Fig. 7(a), showcasing typical behavior for materials experiencing active corrosion. The curves comprise two parts: the cathode branch and anode branch, which are associated with the hydrogen evolution reaction and anodic dissolution, respectively [22]. The corrosion potential (E_{corr}) and corrosion current densities (i_{corr}) are determined through the curve fitting. For the as-cast alloy, the E_{corr} and i_{corr} are −1.519 V and 73.62 μA·cm^{-2}, respectively. The i_{corr} (μA·cm^{-2}) correlates with the average corrosion rate (P_i) using the equation: P_i=22.85i_{corr} [23], yielding a P_i of 1.68 mm·y^{-1} for as-cast alloy. After annealing treatment, the E_{corr} values of WC-LAZ832, AC-LAZ832, and FC-LAZ832 alloys are −1.491 V, −1.530 V, and −1.534 V, respectively. Notably, the WC-LAZ832 alloy exhibits the most positive corrosion potential, indicating the smallest corrosion driving force compared to the other two alloys. The i_{corr} values of the WC-LAZ832 alloy, AC-LAZ832 alloy, and FC-LAZ832 alloy are 23.89 μA·cm^{-2}, 47.42 μA·cm^{-2}, and 100.60 μA·cm^{-2}, respectively, and WC-LAZ832 alloy exhibits the smallest corrosion current density. Furthermore, Fig. 7(b) illustrates the hydrogen evolution rate of the as-cast and annealed Mg-8Li-3Al-2Zn alloys. The WC-LAZ832 alloy also exhibits the lowest rate, signifying superior corrosion resistance among other specimens, corresponding to the electrochemical test results.

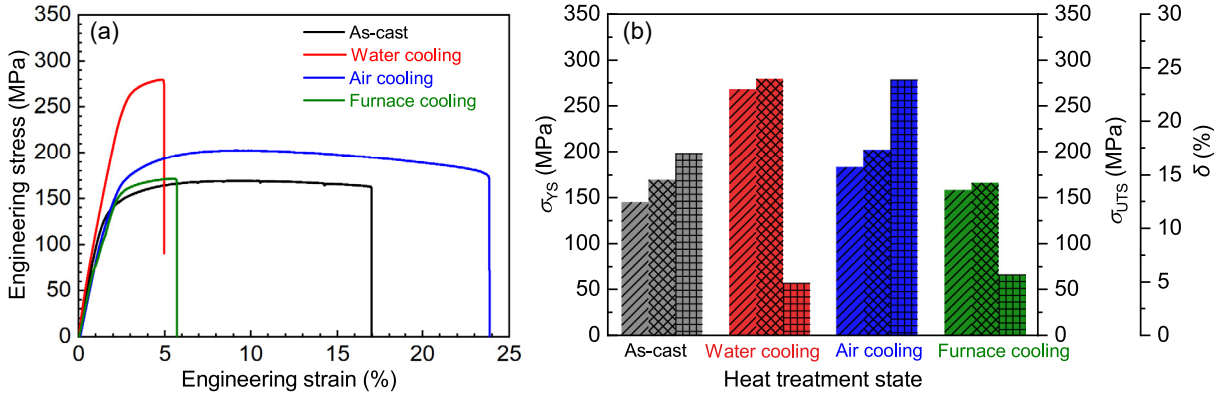

Fig. 5: Stress-strain curve (a), ultimate tensile strength (σ_{UTS}), yield strength (σ_{YS}), and elongation (δ) as a function of *x* (b) for LAZ832 alloy with and without annealing treatment

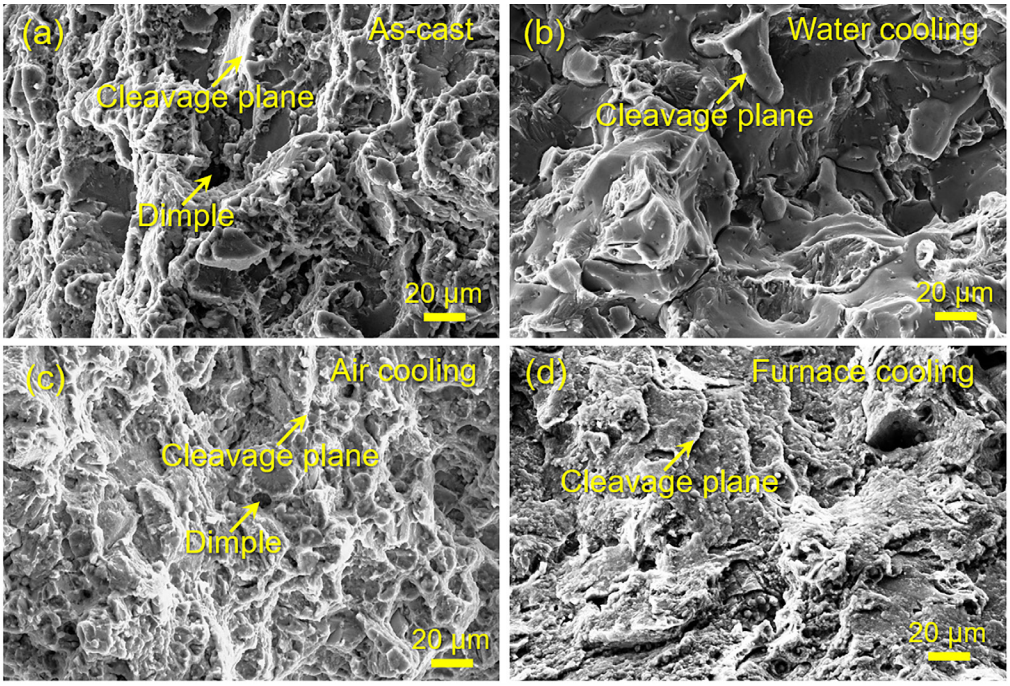

Fig. 6: Tensile fracture morphology of LAZ832 alloy with and without annealing treatment: (a) as-cast; (b) water cooling; (c) air cooling; (d) furnace cooling

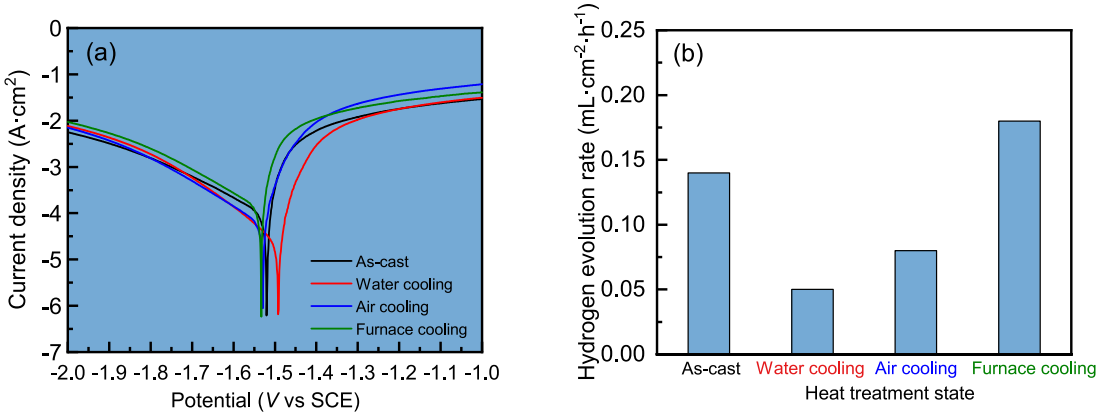

Fig. 7: Polarization curves of as-cast and annealed LAZ832 alloys after immersion in a NaCl solution for 60 min (a), and the hydrogen evolution rate of as-cast and annealed LAZ832 alloys (immersion testing 10 h) (b)

Figure 8 presents the corrosion surface profile image of the as-cast and annealed Mg-8Li-3Al-2Zn alloys after immersion in a NaCl solution for 60 min. Severe and inhomogeneous corrosion is observed on the surface of the as-cast alloy, as shown in Fig. 8(a). In contrast, a reduction in the corrosion product content is observed on the surface of WC-LAZ832 alloy and AC-LAZ832 alloy, indicating improved corrosion resistance. However, when cooled in the furnace, the FC-LAZ832 alloy displays more pronounced corrosion compared to the as-cast alloy, showing the poorest corrosion resistance. Figure 9 presents the SEM micrographs using secondary electron images of as-cast and annealed LAZ832 alloys after immersion for 10 h. As can be seen, the oxidation product of the as-cast LAZ832 alloy exhibits thick and large micro-blocks on the surface. Compared with the as-cast LAZ832 alloy, the oxidation product of WC-LAZ832 alloy and AC-LAZ832 alloy displays fine and even crackles, also demonstrating enhanced corrosion resistance. However, the oxidation production formed on the FC-LAZ832 alloy after immersion is characterized by a thicker oxide film with larger micro-blocks present on its surface, indicating poor corrosion resistance.

4 Discussion

In LAZ832 alloys, there is free of deformation and the average size of γ phases are very large, which indicates that grain refinement and deformation strengthening can be reasonably neglected. Therefore, the variations in mechanical properties and corrosion resistance observed in LAZ832 alloys are closely related to the microstructural evolutions during annealing treatment. These changes can be attributed to two main factors: (1) changes in the degree of solid solution; (2) the volume fraction and size of second phase. In this section, the strengthening mechanism and corrosion mechanism of LAZ832 in different states will be discussed concentrating on these two aspects.

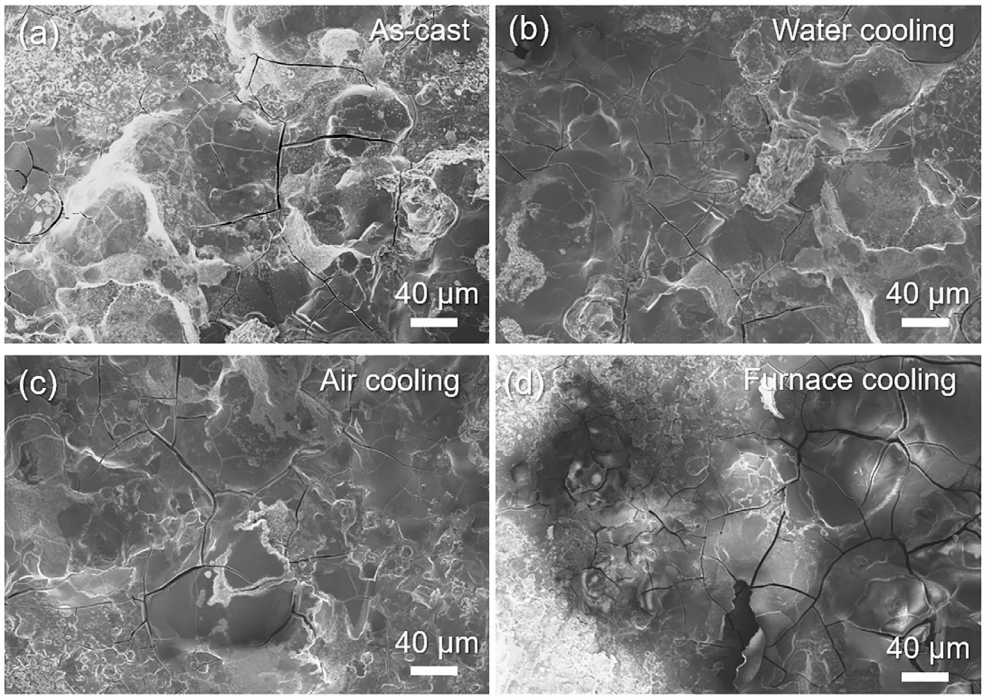

Fig. 8: Corrosion surface profile images of as-cast (a) and annealed (b–d) LAZ832 alloys after immersion in a NaCl solution for 60 min

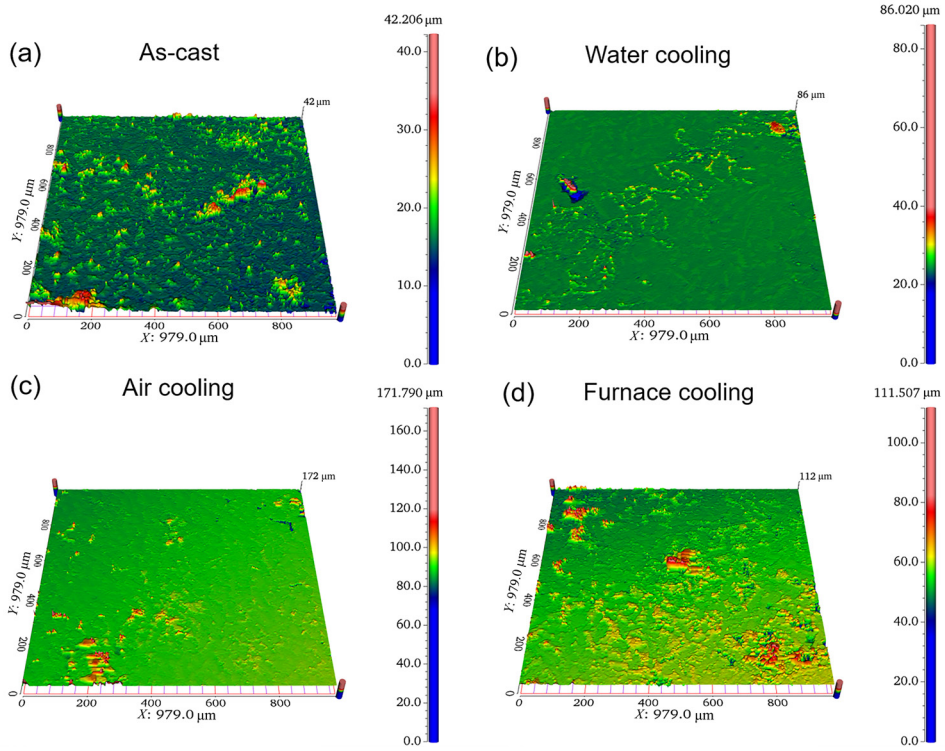

Fig. 9: SEM micrographs secondary electron image of as-cast (a) and annealed (b–d) LAZ832 alloys after immersion for 10 h

4.1 Contributions of strengthening mechanism during annealing treatment

For both as-cast and annealed LAZ832 alloys, the average grain size is large, the effect of fine grain strengthening and deformation strengthening can be reasonably neglected. Hence, the reinforcement of these alloys (σ_{total}) is attributed to solid solution ($\Delta\sigma_{ss}$) and precipitation ($\Delta\sigma_p$) strengthening, expressed as follows [24, 25]:

$$\sigma_{total}=\sigma_0+\Delta\sigma_{ss}+\Delta\sigma_p \quad (2)$$

$$\Delta\sigma_{ss}=M\times\frac{G\times\varepsilon_s^{3/2}\times C^{1/2}}{700} \quad (3)$$

$$\varepsilon_s=\left|\frac{\varepsilon_G}{1+\frac{|\varepsilon_G|}{2}}-3\varepsilon_a\right| \quad (4)$$

$$\Delta\sigma_P = 0.9\frac{\left[\ln\left(\frac{d\pi}{b}\right)^{\frac{3}{2}}\right]}{\left[\ln(L-b)^{\frac{1}{2}}\right]}\left[\frac{Gb}{2\pi(1-\upsilon)\left(L-\left(\frac{\pi}{4}d\right)\right)}\right] \quad (5)$$

where σ_0 represents the lattice frication stress of pure Cu, M is the Taylor factor, c is molar ratio of Al and Zn, G is the shear modulus of matrix, ε_s is the interaction parameter combining the modulus misfit effect and the lattice distortion effect. ε_G and ε_a represent the effects of elastic and atomic size mismatches, respectively. b is the Burgers vector; d and L are size of second phase and the distance between two second phase, respectively, and υ is the Poisson ratio.

For the annealed alloy, when cooled in water, the AlLi phase starts to decompose, and the Al and Zn atoms dissolve into the matrix. The elastic interaction between solute atoms and dislocations, along with the segregation of Al and Zn atoms in the stacking fault zone, impedes dislocation movement on the slip surface. This results in an enhancement of tensile strength and a reduction in elongation of WC-LAZ832 alloy [26]. With a decrease in the cooling rate, the Al and Zn atoms precipitate as the $MgLi_2Al$ phase, gradually transforming into the AlLi phase, thereby reducing the alloy's strength [27]. Notably, an increase in the volume fraction and size of the AlLi phase can be found in the FC-LAZ832 alloy, making it more prone to fracture. Consequently, both the tensile strength and elongation decrease in the alloy.

4.2 Effect of matrix phase and second phase on corrosion behavior

The corrosion behavior of alloys is mainly determined by microstructure evolution. In the present work, the standard electrode potential of Mg (–2.37 V vs. SHE) is more positive than that of Li (–3.02 V vs. SHE) [28]. Therefore, the β-Li matrix is more susceptible to corrosion compared to the α-Mg matrix in the LAZ832 alloy. Furthermore, the electrochemical potential of the AlLi phase (–1.96 V vs. SHE) is more negative than that of the β-Li matrix (–1.26 V vs. SHE) [29], resulting that the AlLi phase more susceptible to corrosion and will preferentially corrode, as the anode in a micro-galvanic corrosion process. This sacrificial corrosion of the AlLi phase protects the α-Mg and β-Li matrices, which act as cathodes, from corrosion. The volume fraction of the AlLi phase in the WC-LAZ832 alloy is significantly reduced compared to the as-cast LAZ832 alloy, which diminishes the possibility of forming micro-galvanic couples and thereby enhances corrosion resistance. During the annealing process, as the cooling rate decreases, the volume fraction of the AlLi phase increases. This increase in the AlLi phase detrimentally affects the corrosion resistance of the alloy, making it even more susceptible to corrosion than the as-cast alloy.

The corrosion behavior of metals inherently involves a series of chemical reactions and charge exchange at the solid solution interface, closely tied to the transport of ions and electrons [30]. The work function, defined as the minimum energy required to remove an electron from the solid, is not only related to the atomic bond strength but also the chemical stability or the efficiency of charge transfer [31, 32]. Accordingly, alloy corrosion theoretically depends on electron characteristics quantifiable by work function. A large work function value corresponds to a more stable electron energy state, contributing to better corrosion resistance. In this study, SPM analysis on the surface potential and work function were conducted to directly reflect the stability of alloy specimens, as shown in Fig. 10.

The distribution of surface potential in both the as-cast and annealed LAZ832 alloys, as shown in Figs. 10(a–b), is associated with compositional fluctuations in the region, allowing for a direct assessment of homogeneity. Compared to the as-cast alloy, the average value of surface potential decreases in the WC-LAZ832 alloy, indicating improved stability of the alloy. Conversely, with the decrease in cooling rate, the average value of surface potential increases, which means

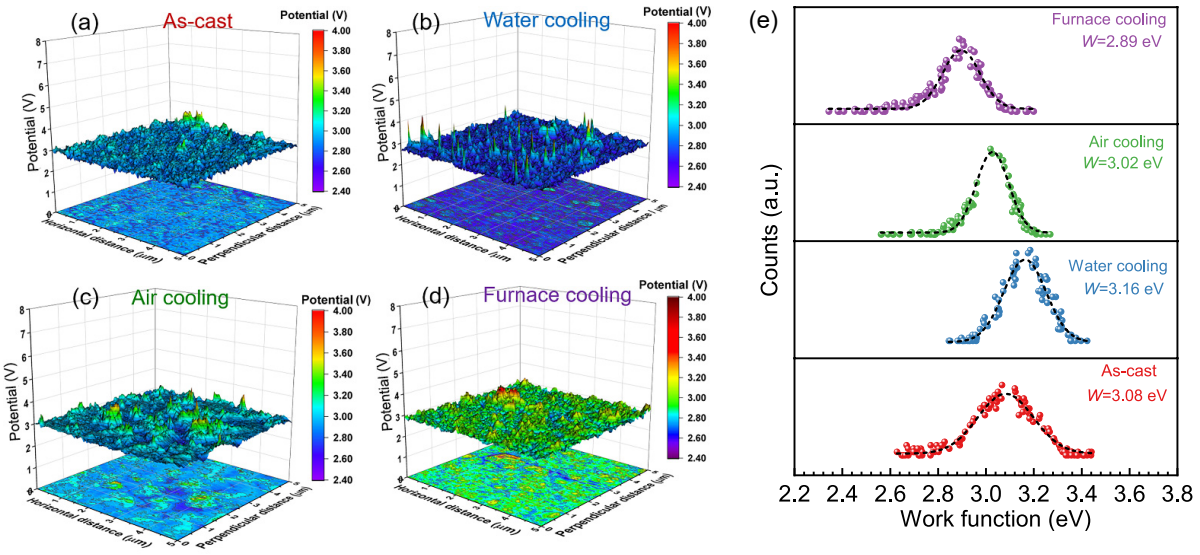

Fig. 10: Surface potential distribution (a–d) and work function (e) of LAZ832 alloy with and without annealing treatment

worse stability. Figure 10(e) presents the evolution of the work function for the as-cast and annealed alloys. For the as-cast alloy, the work function is equal to 3.08 eV. After annealing treatment and subsequent water cooling, the value is increased to 3.16 eV. In contrast, as the cooling rate decreases, the value decreases to 3.02 eV and 2.89 eV in the AC-LAZ832 and FC-LAZ832 alloy, respectively. Therefore, both surface potential distribution and work function depend on the evolution of microstructure. The work function of Mg, Li, Al, and Zn is 3.66, 2.9, 4.28, and 4.33 eV, respectively [33]. After annealing treatment and subsequent water cooling, a significant amount of Al and Zn atoms dissolves into the matrix phase, causing the increase of work function of the matrix, which is beneficial for the improvement of corrosion resistance. When cooled at a slower rate, the Al and Zn atoms precipitate as Al-Li phase, thus leading to the decreased work function and weakening corrosion resistance.

Air cooling was found to achieve an optimal balance between mechanical properties and corrosion resistance. The outcomes of this study provide a theoretical and empirical foundation for the development of Mg-Li alloys with superior comprehensive characteristics.

5 Conclusions

This study systematically investigated the effects of cooling rates on the microstructure and comprehensive properties of Mg-8Li-3Al-2Zn (LAZ832) alloy during annealing, aiming to optimize heat treatment processes for enhanced performance. The main findings of this research are summarized below:

(1) Both as-cast and annealed LAZ832 alloys are composed of α-Mg, β-Li, AlLi, and $MgLi_2Al$ phases. A slower cooling rate (e.g., furnace cooling) promotes the growth and volume fraction of Al-Li intermetallic phases (AlLi and $MgLi_2Al$), while rapid cooling (water quenching) suppresses their precipitation.

(2) The enhanced tensile strength in annealed LAZ832 alloys arises from synergistic solid solution and precipitation strengthening. Solid solution strengthening, driven by the dissolution of Al and Zn atoms into the matrix, dominates the mechanical performance. However, excessive solute content significantly compromises ductility. Air-cooled samples achieve an optimal balance between strength and ductility.

(3) The volume fraction and size of AlLi phases critically influence corrosion resistance. WC-LAZ832 exhibits the lowest corrosion current density due to minimized AlLi phase formation, whereas furnace-cooled samples show accelerated corrosion. Surface potential analysis via atomic force microscopy confirms that Al/Zn dissolution elevates the work function, correlating with improved corrosion resistance through stabilized electron states.

(4) Air cooling emerges as a balanced strategy to tailor LAZ832 alloys for multi-property optimization, offering acceptable strength, enhanced ductility, and moderate corrosion resistance.

Acknowledgments

We would like to gratefully acknowledge the financial support of the Scientific Research Starting Foundation of Anhui Polytechnic University of China (Grant No. 2200YQQ049) and the Excellent Scientific Research and Innovation Teams of Anhui Province, China (Grant No. 2022AH010059).

Conflict of interest

The authors declare that they have no known competing financial interests or personal relationships that could have appeared to influence the work reported in this paper.

References

[1] Yang Y, Xiong X M, Chen J, et al. Research advances in magnesium and magnesium alloys worldwide in 2020. Journal of Magnesium and Alloys, 2021, 9(3): 705–747. https://doi.org/10.1016/j.jma.2021.04.001.

[2] Atrens A, Shi Z M, Mehreen S U, et al. Review of Mg alloy corrosion rates. Journal of Magnesium and Alloys, 2020, 8(4): 989–998. https://doi.org/10.1016/j.jma.2020.08.002.

[3] Luo Q, Guo Y L, Liu B, et al. Thermodynamics and kinetics of phase transformation in rare earth-magnesium alloys: A critical review. Journal of Materials Science and Technology, 2020, 44: 171–190. https://doi.org/10.1016/j.jmst.2020.01.022.

[4] Ma X C, Jin S Y, Wu R Z, et al. Corrosion behavior of Mg-Li alloys: A review. Transactions of Nonferrous Metals Society of China, 2021, 31(11): 3228–3254. https://doi.org/10.1016/S1003-6326(21)65728-X.

[5] Peng X, Liu W C, Wu G H, et al. Plastic deformation and heat treatment of Mg-Li alloys: A review. Journal of Materials Science and Technology, 2022, 99:193–206. https://doi.org/10.1016/j.jmst.2021.04.072.

[6] Zeng Z R, Zhou M R, Esmaily M, et al. Corrosion resistant and high-strength dual-phase Mg-Li-Al-Zn alloy by friction stir processing. Communications Materials, 2022, 3(1): 1–10. https://doi.org/10.1038/s43246-022-00245-3.

[7] Gao W J, Dong X L, Fan Y H, et al. A comparative study on the microstructure, texture, and mechanical properties of extruded Mg-9Li and Mg-9Li-0.3Ca alloys. Materials Science and Engineering: A, 2022, 854: 143844. https://doi.org/10.1016/j.msea.2022.143844.

[8] Li C Q, He Y B, Huang H P. Effect of lithium content on the mechanical and corrosion behaviors of HCP binary Mg-Li alloys. Journal of Magnesium and Alloys, 2021, 9(2): 569–580. https://doi.org/10.1016/j.jma.2020.02.022.

[9] Cain T W, Labukas J P. The development of β phase Mg-Li alloys for ultralight corrosion resistant applications. npj Materials Degradation, 2020, 4(1): 17. https://doi.org/10.1038/s41529-020-0121-2.

[10] Nene S S, Kashyap B P, Prabhu N, et al. Microstructure refinement and its effect on specific strength and bio-corrosion resistance in ultralight Mg-4Li-1Ca (LC41) alloy by hot rolling. Journal of Alloys and Compounds, 2014, 615: 501–506. https://doi.org/10.1016/j.jallcom.2014.06.151.

[11] Guo Y H, Wang W C, Huang H Q, et al. Effect of doping Zn atom on the structural stability, mechanical and thermodynamic properties of AlLi phase in Mg-Li alloys from first-principles calculations. Philosophical Magazine, 2020, 100(14): 1849–1867. https://doi.org/10.1080/14786435.2020.1742397.

[12] Li C Q, Liu X, Dong L J, et al. Simultaneously improved mechanical strength and corrosion resistance of Mg-Li-Al alloy by solid solution treatment. Materials Letters, 2021, 301: 130305. https://doi.org/10.1016/j.matlet.2021.130305.
[13] Zhu Y X, Song G L, Wu P P, et al. A burnished and Al-alloyed magnesium surface with improved mechanical and corrosion properties. Corrosion Science, 2021, 184: 109395. https://doi.org/10.1016/j.corsci.2021.109395.
[14] Zhao J, Li Z Q, Liu W C, et al. Influence of heat treatment on microstructure and mechanical properties of as-cast Mg-8Li-3Al-2Zn-*x*Y alloy with duplex structure. Materials Science and Engineering: A, 2016, 669: 87–94. https://doi.org/10.1016/j.msea.2016.05.085.
[15] Zhu Y X, Chen G Q, Zhou Y F, et al. Achieving synergistic strength-ductility-corrosion optimization in Mg-Li-Al-Zn alloy via cross-pass friction stir processing. Journal of Alloys and Compounds, 2023, 959: 170581. https://doi.org/10.1016/j.jallcom.2023.170581.
[16] Wu J Y, Zhao D L, Lee B, et al. Effect of lithium and aluminum on the mechanical properties, in vivo and in vitro degradation, and toxicity of multiphase ultrahigh ductility Mg-Li-Al-Zn quaternary alloys for vascular stent application. ACS Biomaterials Science and Engineering, 2020, 6(4): 1950–1964. https://doi.org/10.1021/acsbiomaterials.9b01591.
[17] Xue M S, Yao Y, Ou J F, et al. Effect of surface roughness on electron work function of AZ31 Mg alloy and their correlation. Journal of Alloys and Compounds, 2018, 731: 44–48. https://doi.org/10.1016/j.jallcom.2017.10.007.
[18] Ignacio L S, Dong C L, Young D K. Ag nanoparticles on highly ordered pyrolytic graphite (HOPG) surfaces studied using STM and XPS. Surface Science, 2005, 588(1–3): 6–18. https://doi.org/10.1016/j.susc.2005.05.021.
[19] Liang X L, Peng X, Ji H, et al. Microstructure and mechanical properties of as-cast and solid solution treated Mg-8Li-*x*Al-*y*Zn alloys. Transactions of Nonferrous Metals Society of China, 2021, 31(4): 925–938. https://doi.org/10.1016/S1003-6326(21)65550-4.
[20] Li Y, Guan Y J, Liu Y, et al. Microstructure and tensile properties of the friction stir processed LA103Z alloy. Materials Characterization, 2023, 196: 112616. https://doi.org/10.1016/j.matchar.2022.112616.
[21] Sun Y H, Wang R C, Ren J, et al. Microstructure, texture, and mechanical properties of as-extruded Mg-*x*Li-3Al-2Zn-0.2Zr alloys (*x*=5, 7, 8, 9, 11 wt.%). Materials Science and Engineering: A, 2019, 755: 201–210. https://doi.org/10.1016/j.msea.2019.04.007.
[22] Dobkowska A, Adamczyk-cieślak B, Kuc D, et al. Influence of bimodal grain size distribution on the corrosion resistance of Mg-4Li-3Al-1Zn (LAZ431). Journal of Materials Research and Technology, 2021, 13: 346–358. https://doi.org/10.1016/j.jmrt.2021.04.078.
[23] Shi Z M, Liu M, Atrens A. Measurement of the corrosion rate of magnesium alloys using Tafel extrapolation. Corrosion Science, 2010, 52(2): 579–588. https://doi.org/10.1016/j.corsci.2009.10.016.
[24] Gerold V, Haberkorn H. On the critical resolved shear stress of solid solutions containing coherent precipitates. Physica Status Solidi, 1966, 16(2): 675–684. https://doi.org/10.1002/pssb.19660160234.
[25] Heilmaier M, Leetz U, Reppicb H. Order strengthening in the cast nickel-based superalloy IN 100 at room temperature. Materials Science and Engineering: A, 2001, 319: 375–378. https://doi.org/10.1016/S0921-5093(01)00989-3.
[26] Gao L, Chen R S, Han E H. Effects of rare-earth elements Gd and Y on the solid solution strengthening of Mg alloys. Journal of Alloys and Compounds, 2009, 481(1–2): 379–384. https://doi.org/10.1016/j.jallcom.2009.02.131.
[27] Guo X Y, Wu R Z, Zhang J H, et al. Influences of solid solution parameters on the microstrucuture and hardness of Mg-9Li-6Al and Mg-9Li-6Al-2Y. Materials and Design, 2014, 53: 528–533. https://doi.org/10.1016/j.matdes.2013.07.011.
[28] Kumar V, Shekhar R, Balani K, et al. Corrosion behavior of novel Mg-9Li-7Al-1Sn and Mg-9Li-5Al-3Sn-1Zn alloys in NaCl aqueous solution. Journal of Materials Engineering and Performance, 2015, 24: 4060–4070. https://doi.org/10.1007/s11665-015-1687-7.
[29] Lin M C, Tsai C Y, Uan J Y. Electrochemical behaviour and corrosion performance of Mg-Li-Al-Zn anodes with high Al composition. Corrosion Science, 2009, 51(10): 2463–2472. https://doi.org/10.1016/j.corsci.2009.06.036.
[30] Punburi P, Tareelap N, Srisukhumbowornchai N, et al. Correlation between electron work functions of multiphase Cu-8Mn-8Al and de-alloying corrosion. Applied Surface Science, 2018, 439: 1040–1046. https://doi.org/10.1016/j.apsusc.2018.01.018.
[31] Hua G M, Li D Y. Generic relation between the electron work function and Young's modulus of metals. Applied Physics Letters, 2011, 99(4): 041907. https://doi.org/10.1063/1.3614475.
[32] Liu Z R, Li D Y. The electronic origin of strengthening and ductilizing magnesium by solid solutes. Acta Materialia, 2015, 89: 225–233. https://doi.org/10.1016/j.actamat.2015.01.051.
[33] Skriver H L, Rosengaaed N M. Surface energy and work function of elemental metals. Physical Review: B, 1992, 46(11): 7157. https://doi.org/10.1103/PhysRevB.46.7157.